中国光学（中英文）
Chinese Optics
核心期刊

**Integrated opto-mechanical-thermal optimization and analysis of an all-aluminum space imaging spectrometer**

Huang Dan-heng, LI Zong-xuan, REN Shu-hui, HE Yu-lin, Chartsiriwattana PEARACHAD, NING Jiu-xin, YU Dong-hui

Citation:
Huang Dan-heng, LI Zong-xuan, REN Shu-hui, HE Yu-lin, Chartsiriwattana PEARACHAD, NING Jiu-xin, YU Dong-hui. Integrated opto–mechanical–thermal optimization and analysis of an all–aluminum space imaging spectrometer[J]. *Chinese Optics*, In press. doi: 10.3724/CO.EN–2026–0008
黄丹珩, 李宗轩, 任书慧, 何禹霖, Chartsiriwattana PEARACHAD, 宁久鑫, 于东辉. 全铝合金空间成像光谱仪光机热集成优化与分析[J]. 中国光学, 优先发表. doi: 10.3724/CO.EN–2026–0008

View online: https://doi.org/10.3724/CO.EN–2026–0008

---

**文章编号**　2097-1842(xxxx)x-0001-17

# Integrated opto-mechanical-thermal optimization and analysis of an all-aluminum space imaging spectrometer

Huang Dan-heng[1,2,3], LI Zong-xuan[1,2,3 *], REN Shu-hui[1,3], HE Yu-lin[1,3], Chartsiriwattana PEARACHAD[4], NING Jiu-xin[1,3], YU Dong-hui[1,2,3]

(1. *Changchun Institute of Optics*, *Fine Mechanics and Physics*, *Chinese Academy of Sciences*, *Changchun* 130033, *P.R. China*;

2. *University of Chinese Academy of Sciences*, *Beijing* 100049, *China*;

3. *Jilin Provincial Key Laboratory of Aerospace Advanced Optical Imaging Technology* *Changchun*, *Jilin* 130033, *China*;

4. *Senko Advanced Components (Thailand) Co. Bangkok* 10500, *Thailand*)

* *Corresponding author*, *E-mail*: *lizongxuan@ciomp.ac.cn; Tel.:* +86-186-8664-8612

**Abstract**: All-aluminum opto-mechanical systems are promising for space remote sensing due to their athermal design capability, low cost, and rapid manufacturability. However, in practical engineering, structural constraints under mechanical and thermal loads often induce parasitic stresses within the opto-mechanical assemblies, which subsequently degrade optical stability. To address this, we propose an integrated opto-mechanical optimization scheme for a spectrometer's secondary mirror flexible support. Based on an opto-mechanical-thermal integrated analysis and dimensional sensitivity evaluation under gravity and a 5 °C temperature rise, a Kriging surrogate model was developed. This model integrates fundamental frequency and optical responses to optimize structural dimensions and select the most suitable optimization result. The optimization results demonstrate a 14.2% increase in the fundamental frequency to 204.6 Hz, along with reductions of over 21% in system wavefront aberration under both gravity and thermal loads. Experimental results confirms that the mirror surface root mean square is 0.021 λ (λ = 632.8 nm), and the system wavefront aberration across five fields of view remains consistently below 0.048 λ, fully meeting the technical requirements for stable imaging performance. The proposed method effectively enhances the thermo-mechanical-optical stability of all-aluminum spectrometers and offers a valuable design framework for precision opto-mechanical systems.

**Key words**: space imaging spectrometer; flexible mounts structure; opto-mechanical system optimization; Kriging surrogate model; NSGA-II algorithm; wavefront aberration testing

**收稿日期**:2026-03-04; **修订日期**:xxxx-xx-xx

**基金项目**:泰国国家天文研究所基金资助项目(No. E50364X5XZ)

Supported by the National Astronomical Research Institute of Thailand (NARIT) under Grant No. E50364X5XZ.

# 全铝合金空间成像光谱仪光机热集成优化与分析

黄丹珩[1,2,3], 李宗轩[1,2,3]*, 任书慧[1,3], 何禹霖[1,3], Chartsiriwattana PEARACHAD[4],
宁久鑫[1,3], 于东辉[1,2,3]
（1. 长春光学精密机械与物理研究所 中国科学院, 吉林 长春 130033；
2. 中国科学院大学, 北京 100049；
3. 吉林省航天先进光学成像技术重点实验室, 吉林 长春 130033；
4. 森高先进组件 (泰国) 有限公司, 曼谷 泰国 10500）

**摘要:** 全铝合金光机系统理论上可实现无热化设计, 并兼具低成本与快速响应优势, 在空间遥感领域具有重要应用前景。然而在工程中, 结构约束会使光机结构在力热载荷下引入寄生应力, 导致系统性能失稳。针对该问题, 本文提出一种针对光谱仪反射镜柔性支撑结构的光机集成优化方案。基于光机热集成分析与三向重力和 5 °C 温升工况下的尺寸灵敏度评估, 构建了集成基频与光学响应的优化代理模型, 实现了结构尺寸优化及最优结果的筛选。优化结果显示, 系统基频提升 14.2% 至 204.6 Hz, 同时在重力和热载荷作用下的波前误差降低超过 21%。实验结果表明, 镜面面形均方根值达 0.021 λ (λ = 632.8 nm), 五个视场下的系统波前误差均稳定低于 0.048 λ, 完全满足稳定成像性能的技术要求。该方法有效提升了全铝光谱仪的热-力-光稳定性, 可为精密光机系统的结构设计提供有价值的参考。

**关 键 词:** 空间成像光谱仪; 柔性支撑结构; 光机结构优化; Kriging 代理模型; NSGA-II 算法; 波像差检测
**中图分类号:** V447 **文献标志码:** A **doi:** 10.3724/CO.EN-2026-0008 **CSTR:** 32171.14.CO.EN-2026-0008

## 1 Introduction

Driven by growing needs in meteorological forecasting, resource exploration, and environmental monitoring, space optical remote sensing has become a globally critical technology. Large-aperture, long-focal-length sensors provide high-resolution, wide-area imaging for detailed ground observation. However, their immense size and weight necessitate complex manufacturing, extended development, and high costs. This hinders rapid deployment and delays the creation of comprehensive imaging networks. Recently, small space optical imaging systems have steadily advanced. Their mobility and agility enable quick networking and efficient data delivery, while their compact, lightweight design simplifies manufacturing, drastically reducing development cycles and costs [1-3]. Although small systems generally possess lower resolution than large-aperture sensors, they still meet detailed survey requirements. Integrating them with large, long-focal-length sensors yields complementary benefits. Therefore, researching lightweight, compact space optical remote sensors holds significant application value and poses important engineering challenges.

The reflector is a critical component of space-based reflective optical systems, with its surface shape stability directly impacting the imaging quality of the entire system. Ideally, an optical system can perfectly converge a spherical wavefront from an object point to an image point, forming an undistorted spherical wave. However, in real-world conditions, space remote sensors encounter severe environmental challenges during both launch and on-orbit operation [4]. These include intense vibration and impact loads during launch, as well as prolonged exposure to microgravity and significant temperature fluctuations during orbit maintenance. Such factors induce stress redistribution and thermal deformation of the reflector, which in turn compromise its surface shape stability. As a result, the actual outgoing wavefront deviates from the ideal spherical shape, leading to increased wavefront aberration and unstable imaging quality. Therefore, these demanding conditions pose a significant challenge. Specifically, it remains difficult to maintain stable optical system performance while simultaneously achieving the rapid deployment of space optical remote sensors.

Aluminum-based optical payloads offer several advantages, including a short manufacturing cycle, low cost, mature processing technology, and the ability to meet rapid response requirements [5-6]. Additionally, these payloads enable integrated opto-mechanical design, facilitate athermalization, and improve the optical system's overall temperature adaptability. As a result, a growing body of research on aluminum-based optical systems has emerged, with numerous scholars and institutions achieving significant results in this field. Notable examples of aluminum-based optical systems include the SCUBA-2 infrared camera [7], developed by the UK Astronomy Technology Center (UKATC), which uses nine free-form aluminum reflectors to significantly enhance its optical performance. NASA selected the Pandora mission [8] as part of its Astrophysics Pioneers program, aiming to decipher the atmospheric compositions of exoplanets. The Pandora payload features an all-aluminum Cassegrain telescope with a 450 mm aperture. By leveraging the athermalization properties of aluminum alloy at cryogenic temperatures, the telescope enables simultaneous observations across visible to near-infrared wavelengths. In China, the Xi'an Institute of Optics and Precision Mechanics (XIOPM) successfully demonstrated and verified the on-orbit performance of the Full-Aluminum free-form Imager Telescope (FAIT). The FAIT [9] features a fully aluminum opto-mechanical architecture, with both optical and mechanical components made from aerospace-grade aluminum alloy possessing identical coefficients of thermal expansion, and manufactured via Single Point Diamond Turning technology. This design yields benefits such as low cost, rapid response, and effective athermalization for the optical system.

The aforementioned studies have demonstrated the enormous potential of aluminum alloy materials in realizing low-cost, rapid-response, and athermal optical systems. However, in practical engineering, structural assembly constraints and temperature loads under actual working conditions can still introduce thermo-mechanical stresses that degrade the performance of optical systems. Therefore, structural optimization design is required to mitigate such impacts, making opto-mechanical-thermal integrated analysis technology a crucial design tool. Leveraging opto-mechanical integration analysis, researchers optimize opto-mechanical components by using structural responses or optical system performance as objectives or constraints, often in conjunction with advanced optimization algorithms. For instance, Kihm and Yang [10] achieved lightweight design and flexible support optimization for a 1-meter aperture mirror using opto-mechanical integration analysis combined with a multi-objective genetic algorithm. Wang et al. [11] developed a design method for space remote sensor mirror assemblies that integrates empirical design, topology optimization, and dimensional parameter optimization to achieve an optimal structure. Qin et al. [12] established a rapid multi-objective optimization framework for fully parameterized primary mirror structures based on IPSO-IAGA-BPNN, achieving performance enhancements for spaceborne primary mirrors. Shao [13] used an opto-mechanical integration analysis via software to optimize the structural dimensions of a space optical camera, minimizing line-of-sight and wavefront aberration to achieve an ultra-lightweight design. Zhao et al. [14] proposed an integrated mirror light engine design method based on a Kriging surrogate model combined with topology optimization, achieving an optimal lightweight mirror structure.

This paper focuses on the flexible support structure of the reflector in a space-borne all-aluminum alloy spectrometer and distinguishes itself from prior studies on aluminum optics and general opto-mechanical optimization by presenting a methodology for the design of a flexible support in an all-aluminum imaging spectrometer. A finite element model of the reflector's flexible support is established to analyze how changes in dimensional parameters affect optical performance under static gravity and thermal loads. Furthermore, an optimized surrogate model is constructed for the integrated overall structure of the space spectrometer, using wavefront aberration and the fundamental frequency of the structure under static gravity and thermal loads as response values. The impact of dimensional parameters on the system's wavefront aberration under static gravity and thermal loads is thoroughly investigated to identify key parameters affecting optical performance. Using these response quantities as optimization objectives, a multi-objective optimization of the reflector's flexible support structure dimensional parameters is performed. An optimization model is established, with dimensional parameters as design variables and system performance as objectives, to derive the optimal structural configuration. The rationality of the theoretical design is subsequently validated by measuring the root mean square (RMS) values of surface-shape errors for optical components and the wavefront aberration (WFE) of the spectrometer.

## 2 Optical System and Structural Design of the Spectrometer

### 2.1 Introduction to the Optical System

The optical system of the XX-1 hyperspectral imager, designed for Earth observation in the visible to near-infrared range from 400 nm to 1 000 nm, consists of a fore telescope and an Offner spectroscopic system, as illustrated in Figure 1. The fore telescope adopts an off-axis two-mirror configuration, with its core components comprising off-axis aspherical mirrors (M1, M2) and a flat folding mirror (FM). Incident light first strikes the convex off-axis aspherical mirror M1, which reflects the beam toward the aperture stop aspherical mirror M2. M2 then redirects the beam to the folding mirror FM and subsequently into the Offner spectrometer. The fore telescope forms an image of the incoming light on the incident slit plane.

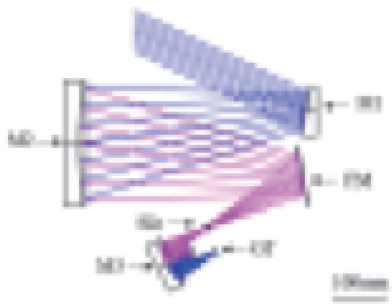

Fig. 1 Two-dimensional layout diagram of the spectrum optical system. M1, M2: Off-axis aspherical mirrors; FM: Folding mirror; M3: Concave spherical mirror; GT: Convex grating.

图 1 光学系统二维光路图 M1、M2: 离轴非球面反射镜; FM: 折叠镜; M3: 球面反射镜; GT: 凸面光栅

Light rays aligned along the slit direction enter the spectrometer, where the concave spherical mirror M3 reflects and collimates the divergent light into a parallel beam. This parallel beam is directed toward the convex grating (GT), which disperses the light, diffracting different wavelengths into distinct directions to generate multiple parallel beams with varying wavelengths. The dispersed beams are reflected again by the concave spherical mirror M3, which focuses them onto the area array detector. At the detector's focal plane, slit images are acquired through continuous spatial push-broom scanning, integrating spatial information with hyperspectral data for comprehensive analysis of target spatial features and spectral characteristics.

To comprehensively evaluate the imaging quality of the system, the full-field Modulation Transfer Function curves across the 400 nm to 1 000 nm spectral band were extracted. As shown in Figure 2, at the spatial frequency of 45 lp/mm, which corresponds to the detector's Nyquist frequency, the full-field Modulation Transfer Function (MTF) values at wavelengths of 400 nm, 500 nm, 600 nm, 700 nm, 800 nm, 900 nm, and 1 000 nm are all greater than 0.5. Additionally, the system achieves a high spectral resolution of 2 nm across the entire working band. This demonstrates that the system fully satisfies the design specifications while retaining an ample margin.

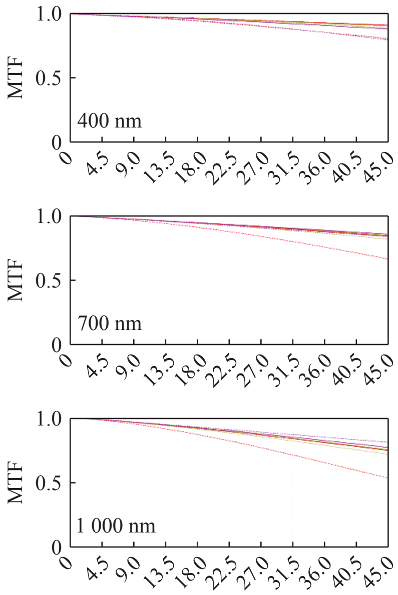


Fig. 2　Modulation Transfer Function of the theoretical system at λ= 400 nm, 500nm, 600nm, 700 nm,800nm, 900nm and 1 000 nm. The frequency varies between 0 cycles/mm and 45 cycles/mm.

图 2　理论系统在波长 λ= 400 nm、500 nm、600 nm、700 nm、800 nm、900 nm 和 1 000 nm 下的调制传递函数。空间频率范围为 0 ~ 45 cycles/mm

Figure 3 illustrates that the maximum smile distortion is -24.8 μm at the field of view (FOV) boundaries. This effect is constant across all wavelengths and can be easily mitigated using standard image processing techniques. Meanwhile, the keystone distortion reaches a maximum of 0.4 μm at the FOV edge at λ= 1 000 nm. This deviation accounts for under 4% of the pixel size, it comfortably meets the acceptable design limits.

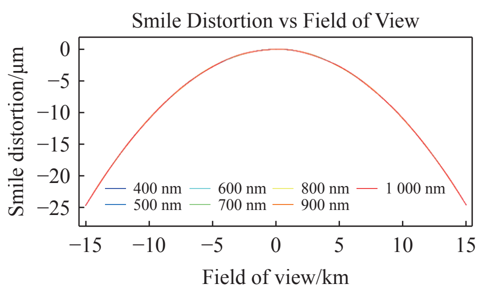


Fig. 3　Theoretical smile distortion of the optical payload.

图 3　光学载荷理论 Smile 畸变

## 2.2　Opto-Mechanical Structural Design

In the design of space mirrors, material selection and configuration are among the core factors that determine the performance and reliability of the entire optical system. In the field of space optical remote sensors, traditional materials such as silicon carbide and glass-ceramic exhibit high specific stiffness. However, their optical components require complex manufacturing processes, including grinding, lapping, and polishing, resulting in long processing cycles and difficulties in controlling position accuracy. Additionally, the high cost of these materials significantly increases the complexity and time required for the assembly of optical systems with ceramic components. In contrast, aluminum-based mirrors overcome these drawbacks and offer excellent machinability. When both the structural frame and optical components are aluminum-based, the mechanical structure can compensate for the thermal defocus of the reflective system. This effectively addresses thermal-mismatch issues caused by the high thermal expansion coefficient of aluminum alloys, achieving athermalization and ensuring good imaging quality over a certain temperature range. Furthermore, this approach substantially shortens the manufacturing cycle and reduces costs.

Therefore, aluminum alloy has become the preferred solution for opto-mechanical systems both domestically and internationally to achieve high reliability and rapid response. Drawing on existing experience, the entire system adopts an all-aluminum opto-mechanical structure. In the structural design, efforts are made to minimize the overall mass and size while ensuring sufficient strength and rigidity. Both the structural frame and mirrors are fabricated from 6061 aluminum alloy. Table 1 compares the properties of 6061 aluminum with those of traditional optical materials (Silicon Carbide and Zerodur), highlighting the thermal and mechanical characteristics relevant to the design. Specifically, the structural frame is produced via additive manufacturing, while the mirror components are manufactured via ultra-precision single-point diamond turning.

**Tab. 1 Comparison of material properties between 6061 and traditional optical materials**

**表 1 6061 与传统光学材料性能对比**

| Material | Density (g/cm$^3$) | Elastic modulus (GPa) | Thermal expansion coefficient ($10^{-6}$ / °C) | Thermal conductivity (W/m·K) |
|---|---|---|---|---|
| AL6061 | 2.70 | 68.9 | 23.6 | 167 |
| SiC | 3.05 | 330 | 2.6 | 180 |
| Zerodur | 2.53 | 90.3 | 0.1 | 1.6 |

The space spectrometer consists of five mirrors, two supporting frames, multiple sets of spacers, and a light shield. The overall optical-mechanical structure of the spectrometer is depicted in Figure 4, with an envelope dimension of 515 mm × 300 mm × 547 mm, meeting the design requirements.

The payload employs a combined active and passive thermal control system, maintaining a temperature control accuracy within ±1 °C to ensure stable operating temperatures. However, in the subsequent opto-mechanical-thermal optimization, we strictly adopted a conservative uniform temperature rise of 5 °C as the boundary condition. This specific margin is intended to account for the degradation of thermal control performance over long-term on-orbit operation, as well as transient thermal shocks and active control lag. Verifying the optical stability under this 5 °C drift provides a reliable safety margin for the system and demonstrates the athermalization capability of the all-aluminum structure.

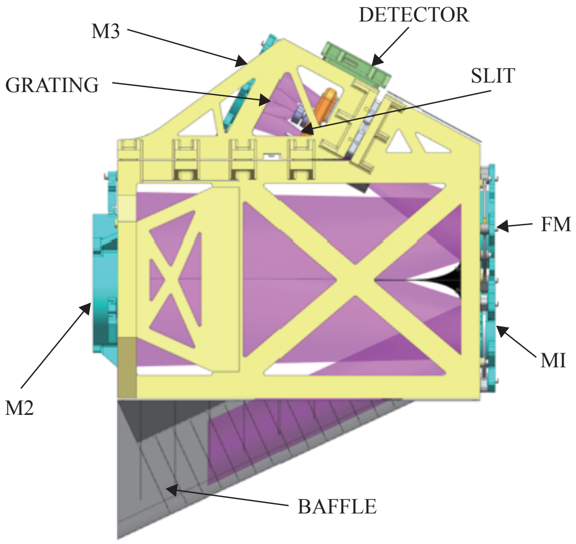


Fig. 4 Overall Structure of the Spectrometer

图 4 光谱仪整体结构图

## 3 Flexible Structure Design of the M2

Due to aluminum's low elastic modulus and high thermal expansion coefficient, optical components made of aluminum are more sensitive to thermo-mechanical loads. To address this, flexible support structures are often used for mirrors, relieving stresses and reducing the impact of thermo-mechanical loads on the mirror surface, thereby achieving stress-free support. By leveraging the properties of metallic materials, an integrated design of the mirror substrate and a flexible support can further improve assembly accuracy and minimize mechanical loading. Common integrated structures for metal mirrors and their flexible supports include back flexible-lug supports and peripheral three-point flexible-lug supports. Figure 5 shows the initial structural design of the M2 mirror, which has a diameter of 245 mm and adopts a peripheral flexible lug support scheme. In this design, three flexible support lugs are uniformly distributed along the circumference of the mirror to relieve thermo-mechanical loads. Five stress relief grooves are sequentially arranged along the radial direction from the mirror center to the outer contour. The first and second grooves, which are parallel to each other and perpendicular to the mounting surface, form the first set of axial flexible hinges to provide Z-direction displacement compensation. The third and fourth grooves constitute the independent second and third sets of radial flexible hinges, respectively, for absorbing thermal deformations in the X-Y plane. The fifth groove serves as the fourth set of axial flexible hinges. These four sets of flexible hinges are connected in series to form a composite hinge for the flexible lugs, enabling three-dimensional thermo-mechanical load relief. To optimize the mirror's dimensional parameters for optimal optical performance in subsequent work, parametric modeling is performed on the designed initial flexible structure. For the first set of flexible hinges, the width and depth of the two flexible grooves are denoted as t1 and h1, respectively. For the second set, the groove width is t2 and the groove length is L2; for the third set, the groove width is t3 and the groove length is L3; for the fourth set, the groove width is t4 and the groove depth is h4, as shown in Figure 5.

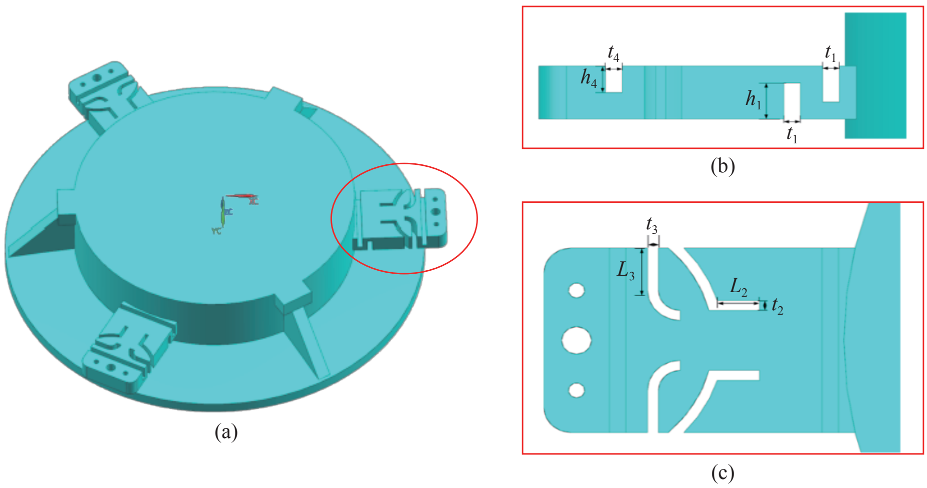


Fig. 5　Schematic diagram of the mirror assembly. (a) Overall structure with the definition of the global coordinate system. (b, c) Enlarged views of the flexible support structure from different angles.

图 5　反射镜组件结构示意图。(a) 带有全局坐标系定义的整体结构; (b, c) 不同角度的柔性支撑结构局部放大图

### 3.1　Sensitivity Analysis of Dimensional Parameters

During structural dimension parameter optimization process, a sensitivity analysis is first conducted for eight key geometric parameters ($t_1/h_1$, $t_2/L_2$, $t_3/L_3$, $t_4/h_4$) under multiple working conditions. A parametric finite element model is established using tetrahedral elements, with mesh refinement applied to the optical surface of the mirror and the flexible support structures. Fixed constraints are applied at the mounting legs of the spectrometer's main support frame to simulate its connection to the satellite platform. Using the finite difference method, a unit perturbation is applied to each parameter individually, considering 1g gravitational loads in the X, Y, and Z directions as well as a uniform temperature rise of 5°C. To accurately quantify the resulting optical performance, opto-mechanical coupling was implemented using the SigFit. The process involves: (1) extracting the deformation data of all surface nodes on the mirror from the FEA results; (2) utilizing SigFit to fit the surface deformation into standard Zernike polynomials; (3) importing the generated Zernike coefficients into the optical design software Zemax to evaluate the variations in wavefront aberration. The sensitivity results for the dimensional parameters with respect to wavefront aberration are presented in Figure 6.

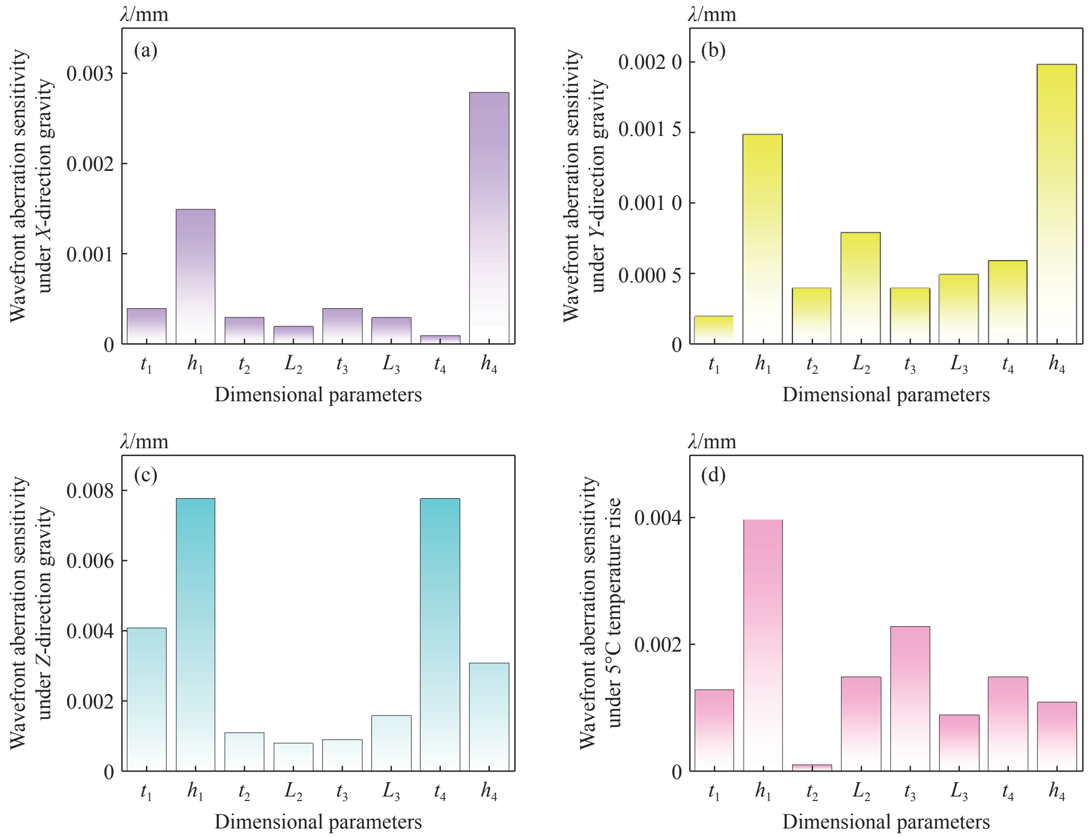


Fig. 6 Wavefront Aberration Sensitivity to Dimensional Parameters. (a) Wavefront Aberration Sensitivity Under X - Direction Gravity; (b) Wavefront Aberration Sensitivity Under Y - Direction Gravity;(c) Wavefront Aberration Sensitivity Under Z - Direction Gravity; (d) Wavefront Aberration Sensitivity Under 5 °C Temperature Rise.

图 6 波前误差对尺寸参数的灵敏度。(a) X 向重力下的波前误差灵敏度; (b) Y 向重力下的波前误差灵敏度; (c) Z 向重力下的波前误差灵敏度; (d) 5 °C 温升下的波前误差灵敏度

Figure 6 illustrates the sensitivity of the system's optical performance to dimensional parameters. As shown in Figure 6(a), under a 1g gravitational load in the X-direction, the groove depths $h_1$ and $h_4$ of the first and fourth sets of flexible hinges have a significant impact, while the other parameters have minimal influence. Figure 6(b) demonstrates that under a 1g gravitational load in the Y-direction, $h_1$ and $h_4$ also show a notable effect on wavefront aberration, with $L_2$ exhibiting some influence as well. In Figure 6(c), under a 1g gravitational load in the Z-direction, $h_1$ and $t_4$ remain the dominant factors, with other parameters having little effect. Figure 6(d) shows that, under a uniform temperature rise of 5 °C, $h_1$ is the most critical parameter affecting wavefront aberration; except for $t_2$, all other parameters show some sensitivity to temperature. In summary, the sensitivity analysis indicates that the groove depths $h_1$ and $h_4$ are the most crucial parameters influencing wavefront aberration, while groove length $L_3$ and groove width $t_2$ have the least relative impact. To simplify the optimization model and enhance computational efficiency, $L_3$ and $t_2$ are fixed at their initial design values in subsequent optimization, focusing analysis and optimization on the six parameters: $h_1$, $h_4$, $t_1$, $L_2$, $t_3$, and $t_4$.

### 3.2 Kriging Model Construction

To optimize the flexible support of the M2 mirror, it is essential to develop a surrogate model that captures the relationship between system input parameters and response values. Given the nonlinear relationship between input parameters and optical responses, constructing a high-precision surrogate model is necessary to replace computationally intensive finite element simulations. Commonly used surrogate modeling techniques include the polynomial response surface method (PRSM), Kriging method, radial basis function (RBF) model, and neural networks. The Kriging surrogate model, originally developed for geostatistics, has been widely adopted in engineering optimization due to continuous advancements. As an interpolation-based model grounded in Gaussian processes, Kriging provides unbiased estimates for unknown points using observed values from known data points. It excels in solving nonlinear problems with high accuracy and is both convenient and flexible for practical applications [15]. In this work, the universal Kriging model is employed, whose output parameter comprises two components: a linear regression part and a stochastic distribution part. The mathematical expression is given by Equation (1):

$$y(x) = f(\beta, x) + z(x) \quad , \qquad (1)$$

Where: $x$ represents the design variable vector; $(x)$ denotes the response value of the Kriging model;

$(\beta, x)$ is the polynomial regression function of variable $x$, representing the global trend model in the design space; $\beta$ is the regression coefficient of the basis function; $z(x)$ is a random function with a mean of 0 and a variance of $\sigma^2$ which represents the local deviation established on the basis of the global approximate simulation. Its covariance equation is expressed as Equation (2):

$$Cov[z(x_i), z(x_j)] = \sigma^2 R(x_i, x_j) \quad , \qquad (2)$$

Where: $x_i, x_j$ denote the $i$-th and $j$-th components of the training samples. $R(x_i, x_j)$ is the correlation function, representing the spatial correlation between sample points. The correlation decreases with the increase of spatial distance, and the Gaussian correlation function is usually adopted, as shown in Equation (3):

$$R(x_i, x_j)=\exp\left(-\sum_{k=1}^{d} \theta_k |x_{i,k} - x_{j,k}|^2\right) \quad , \qquad (3)$$

Where: d denotes the total number of design variables; $x_{i,k}$ and $x_{j,k}$ are the $k$-th components of $x_i, x_j$; The vector $\theta$ is the hyperparameter vector of the Kriging model. $\theta_k$ is the $k$-th component of vector $\theta$, and this parameter reflects the degree of influence of the corresponding variable on the output response.

Based on the dimensional sensitivity analysis results from the previous section, six dimensional parameters ($t_1$, $h_1$, $L_2$, $t_3$, $t_4$, $h_4$) that significantly affect wavefront aberration are selected as design variables for optimization, with the remaining parameters held constant at their initial design values. Before constructing the Kriging surrogate model, it is necessary to select experimental points, as the experimental design sampling strategy directly affects model accuracy and optimization efficiency. Compared to schemes such as full factorial designs, orthogonal experimental designs, and uniform experimental designs, Latin hypercube sampling (LHS) is a stratified sampling method proposed by McKay et al. in 1979 [16]. Its core principle is to divide the interval of each design variable into segments, randomly select one sample point from each segment, and then randomly permute and combine the sample points across variables to form N sets of sampling data, ensuring uniform distribution across each dimension. For multi-dimensional design variables, LHS effectively avoids sample clustering, enhances sampling effectiveness and accuracy, balances randomness and uniformity, and reliably ensures the credibility of analysis results and computational efficiency.

The parameter ranges for the six design variables are specified in Table 2. Using Latin hypercube sampling, 100 sets of sample points are generated for surrogate model construction, and 10 additional detection points are randomly selected to assess model accuracy. The distributions of the sample points for the design variables are depicted in Figure 7. As shown, the sample points are well distributed across the parameter space, which helps ensure the accuracy and reliability of the surrogate model.

**Tab. 2 Value ranges of design variables.**

**表 2 设计变量取值范围**

| Design Variables | Value Range /mm |
|---|---|
| $t_1$ | 1.5-3 |
| $h_1$ | 6-8 |
| $L_2$ | 6-9 |
| $t_3$ | 1.5-2.5 |
| $t_4$ | 1.5-3 |
| $h_4$ | 5-7 |

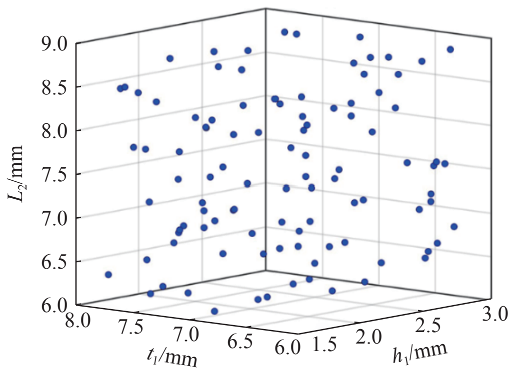


Fig. 7 Distribution Map of Sample Points for Partial Design Variables.

图 7 部分设计变量样本点分布图

### 3.3 Model Accuracy Verification

The optimization process is conducted using the sample points generated from the experimental design. All design variables are normalized, and a Kriging surrogate model is constructed to map the relationship between the six design parameters and the output responses of the space spectrometer's flexible support structure. This model captures the mapping from six design variables to three response values, which cannot be fully visualized in a single plot. Therefore, the Figure 8 presents response fitting surfaces for selected dimensional parameters versus each response value.

The results indicate that different parameters have markedly different effects on the system. For example, as parameter $L_2$ increase, the fundamental frequency of the spectrometer structure also increases, suggesting enhanced seismic performance with these dimensional changes. Meanwhile, a decrease in parameter $t_3$ and an increase in $t_4$ result in a rise in the system's wavefront aberration under Z-direction gravitational load, demonstrating that adjusting these parameters can effectively suppress gravity-induced wavefront aberration deterioration. However, at the global level, the relationships between the six design parameters and the three response values are generally complex and nonmonotonic, with strong parameter coupling.

To verify the predictive reliability of the constructed surrogate model, its accuracy is systematically evaluated. In this study, ten independent validation sample points are generated using the experimental design approach and used to input the established Kriging model to obtain predicted response values. The true response values for these points are then obtained through finite element simulations. The coefficient of determination ($R^2$), calculated using Equation (4), is a quantitative metric used to assess the consistency between predicted and true values.

$$R^2 = 1 - \frac{\sum_{i=1}^{n}(t_i - \hat{t}_i)^2}{\sum_{i=1}^{n}(t - t_i)^2} \quad (4)$$

Where: $t_i$, $\hat{t}_i$ are the simulated value and predicted value of the $i$-th validation point; $t$ is the mean of the simulated values across all validation points; and n is the total number of validation points ($n$ = 10). The value of $R^2$ ranges from 0 to 1. Values closer to 1 indicate higher model fit and better predictive performance. As shown in Table 3, the coefficients of determination for each response value predicted by the Kriging model at the validation points are all greater than 96%, and the predicted values are in close agreement with the simulated values. This indicates that the constructed Kriging model can be reliably used as an approximation of the finite element simulation model for optimization design, as it accurately reflects the mapping relationship between input and output data and demonstrates excellent predictive performance.

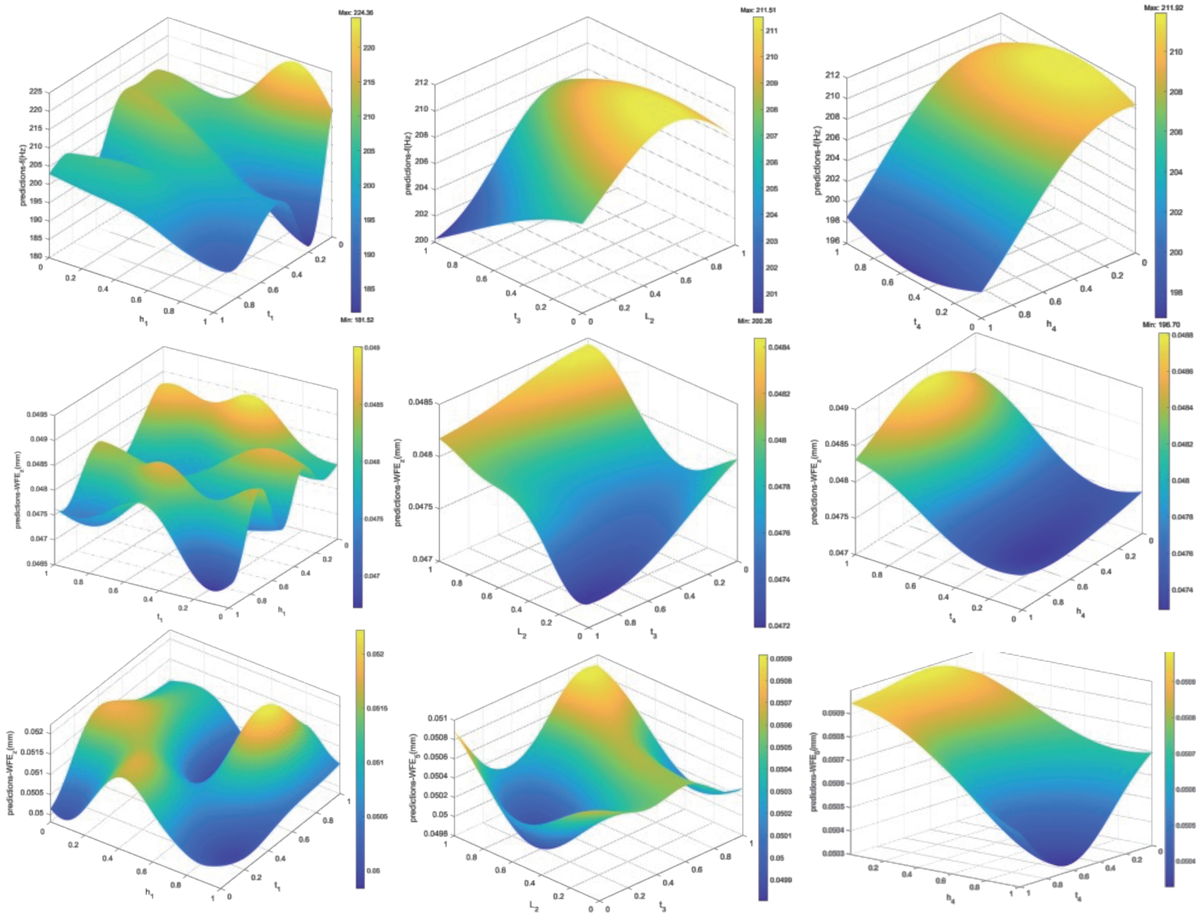

Fig. 8　Fitted Response Surfaces of Partial Design Parameters to Responses.

图 8　部分设计参数对响应值的拟合曲面

**Tab. 3　Coefficient of Determination of Each Response**

**表 3　各响应值的决定系数**

| | f | WFE(z) | WFE(5 °C) |
|---|---|---|---|
| $R^2$ | 0.9811 | 0.9698 | 0.9764 |

## 4　Dimensional Parameter Optimization of the Flexible Support Structure

The aforementioned analysis indicates strong coupling among the dimensional parameters and highly nonlinear relationships between these parameters and target responses. To achieve optimal system performance, this study uses the Non-dominated Sorting Genetic Algorithm II (NSGA-II) to optimize the dimensional parameters within the design space, based on the established surrogate model [17]. By simulating selection, crossover, and mutation operations inspired by biological evolution, NSGA-II conducts a global search to identify a set of non-dominated solutions in complex design spaces [18]. It selects solutions that satisfy the objectives and constraints from the Pareto frontier using the dominance relationship principle.

The mathematical model for the optimization of the flexible support dimensional parameters is defined in Equation (5):

$$\begin{array}{c}\text{Design Variables:}\\ x=[t_1,h_1,L_2,t_3,t_4,h_4]^T\\ \text{Objective Functions:}\\ max f(x)\\ min WFE_Z(x)\\ min WFE_5(x)\\ \text{Constraints:}\\ f(x)\geqslant 100\text{Hz}\\ \begin{cases}1.5\leqslant t_1\leqslant 3\\ 6\leqslant h_1\leqslant 8\\ 6\leqslant L_2\leqslant 9\\ 1.5\leqslant t_3\leqslant 2.5\\ 1.5\leqslant t_4\leqslant 3\\ 5\leqslant h_4\leqslant 7\end{cases}\end{array} \tag{5}$$

The population size is set to 200, and the number of generations is set to 300 for the NSGA-II optimization in the six-dimensional design space. Regarding the population size, a relatively conservative strategy was adopted to ensure global convergence. This setting aims to maximize population diversity in order to adequately cover the broad six-dimensional design space. Regarding the number of generations, full advantage was taken of the computational efficiency of the Kriging surrogate model. Unlike direct finite element-based optimization, which is computationally expensive, the surrogate model enables rapid function evaluations. Therefore, the maximum number of generations was set to 300. Thanks to the computational efficiency afforded by the surrogate model, the optimization process can perform many iterations in a short time. This allows for comprehensive exploration of the design space and the acquisition of a high-quality Pareto optimal solution set, as illustrated in Figure 9.

The Pareto frontier reveals a trade-off between the three objective functions: pursuing a higher fundamental frequency typically comes at the expense of optical performance. To select the final design from the Pareto solution set, hard index screening, comprehensive performance trade-offs, and engineering feasibility are considered. The chosen scheme ensures that the structural fundamental frequency meets the required constraints, achieves a balanced compromise among the three objectives without significant drawbacks, and undergoes process rounding of its dimensional parameters. It is verified that the change in system performance after rounding is less than 2%. The optimized and rounded dimensional parameter values for the final solution are listed in Table 4.

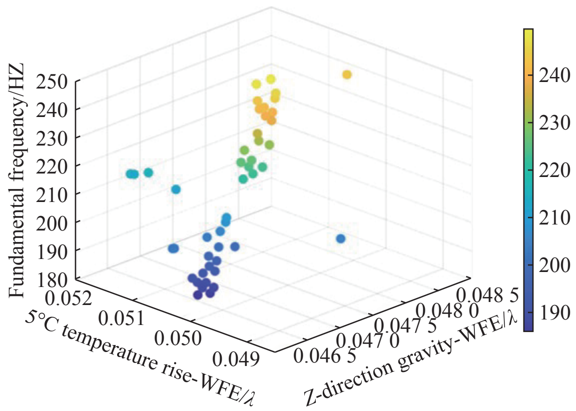


Fig. 9 Three-Dimensional Pareto Front

图 9 三维帕累托前沿图

**Tab. 4 Optimization Results**

**表 4 优化结果**

| Parameter | Optimization Result | Final Result |
|---|---|---|
| $t_1$ | 1.98 | 2 |
| $h_1$ | 7.03 | 7 |
| $L_2$ | 7.87 | 7.8 |
| $t_3$ | 2.22 | 2.2 |
| $t_4$ | 2.63 | 2.6 |
| $h_4$ | 6.07 | 6 |

A finite element model was reestablished, and the optimized scheme was incorporated into the finite element analysis for validation. Performance metrics of the final optimized design were compared with those of the initial configuration, and the comparative results are summarized in Table 5. The data demonstrate that, through this multi-objective optimization approach, both the dynamic stiffness and thermomechanical-optical stability of the spectrometer have achieved significant and balanced improvements, comprehensively surpassing those of the initial design. This validates the effectiveness of the proposed optimization strategy. Furthermore, the wavefront aberrations of the optimized structure under non-optimized conditions also fully satisfy the design requirements, exhibiting no performance degradation.

**Tab. 5 Comparison Before and After Optimization**

**表 5 优化前后对比**

| Performance Indicator | Initial Design | Optimized Design | Improvement Ratio |
|---|---|---|---|
| Fundamental Frequency (Hz) | 178.3 | 204.6 | +14.2% |
| Z-Direction Gravity- WFE (λ) | 0.0601 | 0.0474 | −21.1% |
| 5 °C Temperature Rise-WFE (λ) | 0.0635 | 0.0490 | −22.8% |

## 5 Physical Testing

To practically verify the effectiveness of the integrated opto-mechanical optimization proposed in Section 4, a physical prototype of the M2 mirror assembly was manufactured strictly according to the final optimized dimensional parameters listed in Table 4. Subsequent physical testing, including optical mirror surface inspection and system wavefront aberration testing, was conducted. The primary objective of this section is to verify the engineering manufacturability and evaluate the baseline optical performance of the optimized structure under standard conditions.

### 5.1 Optical Mirror Surface Inspection

A null compensation optical path was established for surface accuracy measurement of the aspherical mirror, comprising a Zygo interferometer and a computer-generated hologram (CGH) compensator, as shown in Figure 10. In this setup, the plane wave emitted by the interferometer is transformed by the CGH into an ideal aspherical wavefront that illuminates the test mirror. Upon reflection, the wavefront acquires surface error information from the test mirror. This modulated wavefront then propagates back through the optical path, where the CGH reconstructs it into a plane wave, allowing it to interfere with the reference beam from the interferometer. The resulting interference fringes encode the surface errors of the mirror, providing a precise measurement basis.

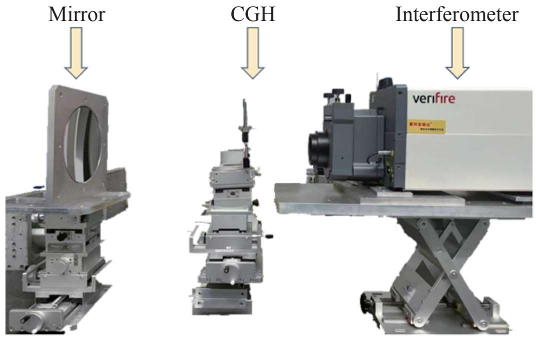


Fig. 10 Photo of mirror assembly surface shape detection.

图 10 反射镜组件面形检测现场

Surface inspection of the mirror is a key method for evaluating the rationality of the flexible support structure design for the mirror assembly. To ensure the initial optical quality, the M2 mirror was fabricated from a 6061-T6 aluminum alloy blank. To minimize the release of internal residual stresses, a strict multi-stage machining and thermal treatment cycle was employed. The final optical surface was generated using an ultra-precision Single Point Diamond Turning machine. In its unconstrained state before installation, the surface figure accuracy of the M2 mirror was measured to be 0.019 λ.

After the flexible support legs were mounted to the frame under actual assembly conditions, the surface inspection was conducted at 20 °C. As shown in Figure 11, the RMS of 0.021 λ and peak-to-valley (PV) of 0.425 λ, meeting the spectrometer technical requirement of RMS≤λ/40 (λ=632.8 nm). The minimal degradation of only 0.002 λ demonstrates that the monolithic flexible support highly effectively isolates assembly stress. Furthermore, five consecutive tests confirmed measurement stability with deviations below the interferometer's resolution (0.001 λ). This fully confirms that the flexible support structure effectively releases stress, thereby verifying the rationality and effectiveness of the structural design.

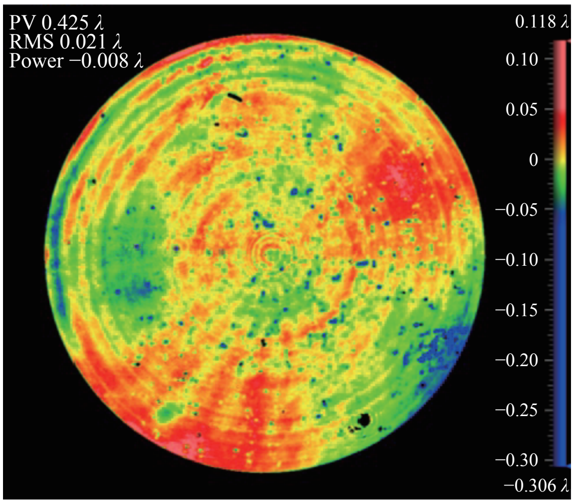


Fig. 11 Testing Results of M2 Mirror

图 11 M2 反射镜检测结果

### 5.2 Wavefront Aberration Testing During Modular Assembly and Alignment

The core principle of wavefront aberration detection is to evaluate the imaging quality of an optical system by measuring the phase deviation between the actual wavefront and the ideal wavefront within the system. In this study, to verify the effectiveness of the preliminary structural optimization, a modular assembly and alignment experiment of the mirror assembly was conducted. The experiment was performed on an optical precision vibration-isolation platform, using a Zygo interferometer and a standard flat mirror to measure the wavefront aberration of the mirror system after precise alignment under the frame-free condition. The experimental principle and test setup are illustrated in Figure 12.

At the start of the detection process, a laser beam emitted from the interferometer forms the reference wavefront for measurement. Each mirror is individually fixed on multi-dimensional adjustment stages according to its spatial position. After the laser beam enters the mirror system under test, the interferometer is used to finely adjust the pitch and yaw of each mirror sequentially until all mirrors reach the optimal positions specified by the optical design. Following sequential reflection by the mirrors, the beam finally propagates to the standard mirror. The beam is then reflected by the standard mirror and returns along the original optical path, re-entering the interferometer.

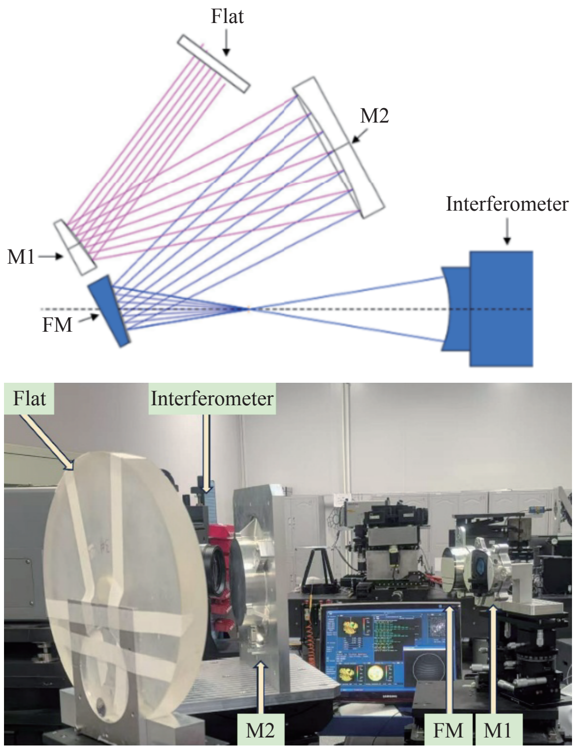


Fig. 12 Principle of Wavefront Aberration Detection and Experimental Site Diagram.

图 12 波前误差检测原理及实验现场

During the experiment, the position and orientation of each mirror assembly are repeatedly fine-tuned, while the real-time interference pattern is observed. An interference pattern with clear features, symmetry, and the minimum number of fringes is obtained in the field of view. The interferometer then acquires and records stable wavefront phase data.

To evaluate the optical system's performance across the full field of view, after completing central field-of-view alignment and measurement, wavefront aberration is detected at different field-of-view (FOV) points. The incident beam angle on the mirror system is adjusted by precisely modifying the standard mirror's position to simulate off-axis FOV conditions. By systematically varying the standard mirror's pose, a series of wavefront aberration distributions across different FOVs is obtained, as shown in Figure 13. Similar repeatability tests confirmed the system's stability. The detailed quantitative results are summarized in Table 6. As shown in Table 6, the RMS values exhibit high consistency across the full FOV, stabilizing around 0.045 λ. The PV values range from 0.299 λ to 0.459 λ. The measured PV values satisfy the design requirements, and the stable RMS performance confirms the robustness of the opto-mechanical structure under gravity.

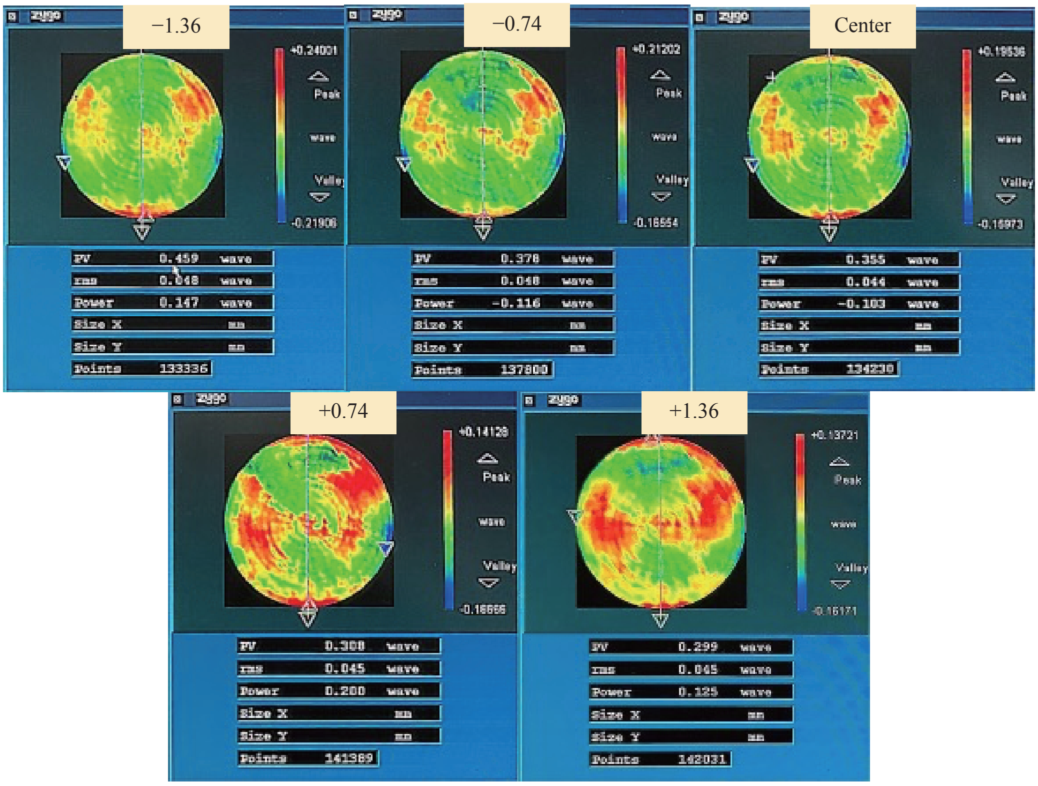


Fig. 13 Wavefront aberration detection cloud maps under different fields of view.

图 13 不同视场下的波前误差检测云图

**Tab. 6 Wavefront aberration detection results under different fields of view**

**表 6 不同视场下的波前误差检测结果**

| FOV | −1.36° | −0.74° | Center | +0.74° | +1.36° |
|---|---|---|---|---|---|
| PV | 0.459 λ | 0.378 λ | 0.355 λ | 0.308 λ | 0.299 λ |
| RMS | 0.048 λ | 0.048 λ | 0.044 λ | 0.045 λ | 0.045 λ |

## 6 Conclusion

This study addresses the issue of optical system instability in an all-aluminum space spectrometer induced by thermo-mechanical loads. To achieve the desired optical performance, the flexible support structure of the largest mirror in the opto-mechanical system was optimized. Parametric modeling was performed for the 245mm M2 mirror, and a comprehensive opto-mechanical-thermal integrated analysis was conducted for the entire spectrometer structure. The finite element method was used to analyze structural responses under gravitational and thermal loads, and the contributions of each dimensional parameter to the optical response were evaluated.

To optimize optical performance, a surrogate model integrating both the optical response and the fundamental structural frequency was established. Dimensional parameter optimization was carried out with optical and structural performance as objectives. As a result, both dynamic stiffness and thermo-mechanical-optical stability of the spectrometer were significantly and balancedly improved.

Surface inspection of the mirror was measured using a Zygo interferometer, yielding RMS value of 0.021 λ, outperforming the spectrometer's technical specification of RMS ≤λ/40. For system-level validation, the wavefront aberration RMS values of the optical system were measured using a Zygo interferometer and a standard mirror at five fields of view. The resulting values are 0.048 λ, 0.048 λ, 0.044 λ, 0.045 λ, and 0.045 λ. All measurements comply with the technical requirement of RMS ≤λ/14 for the spectrometer's imaging system. These results verify the rationality and effectiveness of the optimized flexible support structure design for the mirror. The theoretical simulation in Section 4 and the physical testing in Section 5 form a complementary validation: the simulation proves the design's superiority under extreme space conditions, while the physical testing confirms its actual engineering feasibility and baseline performance.

The integrated opto-mechanical-thermal optimization framework proposed in this paper is fundamentally methodology-oriented and inherently general. Its effectiveness has been validated on the all-aluminum spectrometer developed in this study, and its practicality can be readily extended to other precision opto-mechanical systems operating under complex environmental conditions. For optical components with different apertures or structural configurations, the optimization process can be easily adapted by redefining the design variables and capturing the new variable-performance relationships. In summary, this framework provides a standardized and transferable solution for the structural design of high-precision space optical components, demonstrating promising potential for broad applications.

**References:**


[1] 闻新. 太空探索正在进入航天器集群时代[J]. 人民论坛·学术前沿, 2017(5): 19-26.
WEN X. Space exploration is entering the era of spacecraft cluster[J]. *Frontiers*, 2017(5): 19-26. (in Chinese).

[2] 叶钊, 李熹微, 王超, 等. 微纳卫星光学载荷技术发展综述[J]. 航天器工程, 2016, 25(6): 122-130.
YE ZH, LI X W, WANG CH, *et al*.. Survey of technological development of optical payload for micro-nano satellite[J]. *Spacecraft Engineering*, 2016, 25(6): 122-130. (in Chinese).

[3] 沙治波, 俞越, 焦建超. 国外微纳遥感载荷技术最新进展[J]. 航天返回与遥感, 2021, 42(5): 39-48.
SHA ZH B, YU Y, JIAO J CH. The latest development of micro-nano remote-sensing payload technology abroad[J]. *Spacecraft Recovery & Remote Sensing*, 2021, 42(5): 39-48. (in Chinese).

[4] YODER P, VUKOBRATOVICH D. *Opto-Mechanical Systems Design, Volume 1: Design and Analysis of Opto-Mechanical Assemblies*[M]. 4th ed. Boca Raton: CRC Press, 2015.

[5] 王一凡, 余俊, 盛鹏峰, 等. 轻小型铝基光学载荷技术的研究进展[J]. 航天返回与遥感, 2025, 46(1): 45-59.
WANG Y F, YU J, SHENG P F, *et al*.. Research progress in lightweight metal-based optical payload technology[J]. *Spacecraft Recovery & Remote Sensing*, 2025, 46(1): 45-59. (in Chinese).

[6] 孙景旭, 谢虹波, 李淑贤, 等. 轻小型全铝高分相机[J]. 中国光学(中英文), 2023, 16(6): 1450-1462.
SUN J X, XIE H B, LI SH X, *et al*.. All-aluminum high-resolution camera with lightweight and compact size[J]. *Chinese Optics*, 2023, 16(6): 1450-1462. (in Chinese).

[7] HAWARDEN T G, CASALI M M, HOLLAND W S, *et al*. . Wide-field astronomy projects at the UKATC[C]. *Proceedings of the AAS 199th Meeting*, American Astronomical Society, 2002: 1464.

[8] ROTMAN Y, MCGILL P, WELBANKS L, *et al*.. NASA's Pandora SmallSat mission: simulated modeling and retrieval of near-infrared exoplanet transmission spectra[J]. *The Astronomical Journal*, 2026, 171(5): 263.

[9] YU J D, MAO X L, GAO R, *et al*.. Unobscured off-axis three-mirror freeform all-aluminum imaging telescope[J]. *Applied Optics*, 2025, 64(7): 1677-1692.

[10] KIHM H, YANG H S. Design optimization of a 1-m lightweight mirror for a space telescope[J]. *Optical Engineering*, 2013, 52(9): 091806.

[11] 王克军, 宣明, 董吉洪, 等. 空间遥感器反射镜组件结构设计方法[J]. 红外与激光工程, 2016, 45(11): 1113001.
WANG K J, XUAN M, DONG J H, *et al*.. Design method of reflector component structure of space remote sensor[J].

*Infrared and Laser Engineering*, 2016, 45(11): 1113001. (in Chinese).

[12] QIN T, GUO J L, JING Z J, *et al*.. Hybrid IPSO-IAGA-BPNN algorithm-based rapid multi-objective optimization of a fully parameterized spaceborne primary mirror[J]. *Applied Optics*, 2021, 60(11): 3031-3043.

[13] SHAO M Q, ZHANG L, JIA X ZH. Optomechanical integrated optimization of a lightweight mirror for space cameras[J]. *Applied Optics*, 2021, 60(3): 539-546.

[14] ZHAO Y B, LI L. The application of a topology optimization algorithm based on the kriging surrogate model in the mirror design and optimization of an aerial camera[J]. *Sensors*, 2023, 23(16): 7236.

[15] SIMPSON T W, MAUERY T M, KORTE J J, *et al*.. Kriging models for global approximation in simulation-based multidisciplinary design optimization[J]. *AIAA Journal*, 2001, 39(12): 2233-2241.

[16] MCKAY M D, BECKMAN R J, CONOVER W J. A comparison of three methods for selecting values of input variables in the analysis of output from a computer code[J]. *Technometrics*, 1979, 21(2): 239-245.

[17] DEB K, AGRAWAL S, PRATAP A, *et al*. . A fast elitist non-dominated sorting genetic algorithm for multi-objective optimization: NSGA-II[C]. *Proceedings of the 6th International Conference on Parallel Problem Solving from Nature*, Springer, 2000: 849-858.

[18] VERMA S, PANT M, SNASEL V. A comprehensive review on NSGA-II for multi-objective combinatorial optimization problems[J]. *IEEE Access*, 2021, 9: 57757-57791.

Author Biographies：

Dan-heng Huang (2000—), Master, Changchun Institute of Optics, Fine Mechanics and Physics, Chinese Academy of Sciences. Her research focuses on the optomechanical structural optimization and analysis of optical paylo ads.E-mail: huangdanheng23@mails.ucas.ac.cn.

Zong-xuan Li (1986—), Professor, Changchun Institute of Optics, Fine Mechanics and Physics, Chinese Academy of Sciences. His research interests include the overall optomechanical technology for space optical payloads, as well as the integrated dynamic analysis and optimization of optomechanical systems. E-mail: lizongxuan@ciomp.ac.cn